Solvent-Polarity Tuning Excited-State Charge Coupled Proton-Transfer Reaction in *p*-*N*,*N*-Ditolylaminosalicylaldehydes

Pi-Tai Chou,* Wei-Shan Yu, Yi-Ming Cheng, Shih-Chieh Pu, Yueh-Chi Yu, Yu-Chung Lin, Chien-Huang Huang, and Chao-Tsen Chen*

Department of Chemistry, National Taiwan University, Taipei, Taiwan, ROC

Received: April 10, 2004; In Final Form: May 31, 2004

Detailed insight into the excitation behavior for charge versus proton transfer in *p*-*N*,*N*-ditolylaminosalicylaldehyde (**Ia**) has been gained via luminescence spectroscopy and femtosecond dynamics. In cyclohexane, following an ultrafast rate ($\sim 2.0 \times 10^{12}$ s^{-1}) of excited-state intramolecular proton transfer (ESIPT), fast equilibrium takes place between normal (N*) and tautomer excited states (T*), resulting in dual fluorescence maximized at 450 and 540 nm, respectively, with a common population decay rate of 360 ps^{-1}. The normal emission exhibits drastic solvent-polarity dependence and has been concluded to originate from a charge-transfer species incorporating excited-state intramolecular charge transfer from ditolylamine to carbonyl oxygen. In dipolar solvents, competitive rates between ESIPT and solvent relaxation were observed, and the solvated charge-transfer state is thermodynamically more favorable, so that the T* → N* reverse proton transfer takes places. Supplementary support was provided by the corresponding experiments for the methoxy derivative of **Ia** as well as other relevant analogues. The results shed light on detailed proton/charge transfer coupled dynamics as well as the associated solvent-relaxation dynamics at an early time domain.

1. Introduction

Proton transfer[1] represents one of the most fundamental processes involved in chemical reactions as well as in living systems.[2] Vast numbers of research projects have been published regarding various types of proton transfer, among which the excited-state intramolecular proton transfer (ESIPT) has received much attention.[3] Numerous ESIPT molecules have been explored and investigated to shed light on their corresponding spectroscopy and dynamics. Most ESIPT molecules possess either six- or five-membered ring types of strong intramolecular hydrogen bond between O−H (or N−H) and C═O (or pyridinic nitrogen) groups, in which the intrinsic proton transfer in the $^1\pi\pi^*$ state[4] is essentially barrierless in nonpolar solvents[5] and may proceed either during the periods of low frequency, large-amplitude vibrational motions associated with the hydrogen bond[6a] or ballistically, as recently proposed by Lochbrunner.[6b]

In polar solvents, solvent static/dynamic perturbation may play an important role in manipulating ESIPT pathways. On one hand, for ESIPT molecules with a relatively weak intramolecular hydrogen bond, perturbation from solvent polarity, especially protic environments, may modify the ESIPT dynamics via the formation of a solute/solvent hydrogen-bonded complex. As a result, ESIPT may either be prohibited within the excited-state life span or proceed with a prerequisite of (protic) solvent diffusive reorganization.[7] On the other hand, considering the possibly large differences in dipole moment (in terms of orientation and/or magnitude) between excited normal (μ^*_N) and tautomer species (μ^*_T), the normal and tautomer equilibrium polarizations might be far separated. Since the large dipolar change in solution is normally coupled to solvent polarization effects, the relative energetics between normal and tautomer is expected to be a function of solvent polarization coordinate.

SCHEME 1: Energetics as a Function of Solvent Polarization[a]

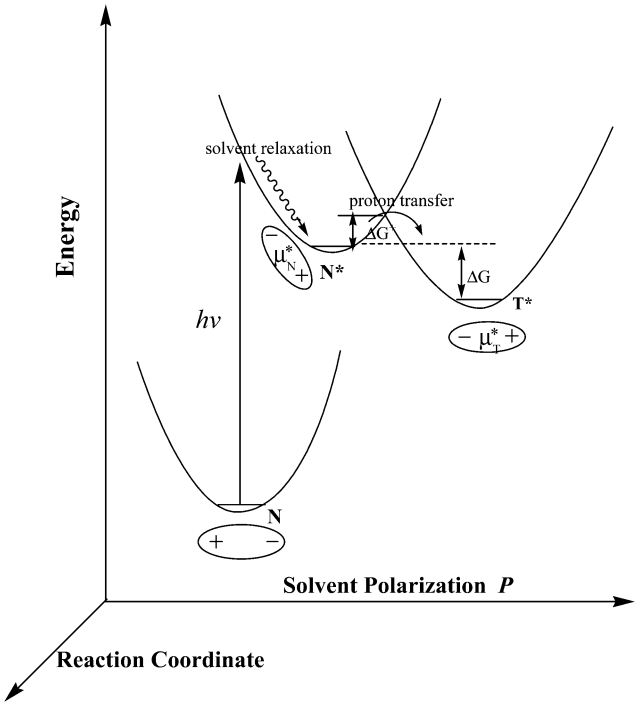

[a] Considering the possibly large differences in dipole moment between excited normal (μ^*_N) and tautomer species (μ^*_T), the normal and tautomer equilibrium polarizations might be far separated. Accordingly, a solvent induced barrier (ΔG^+) may channel into the proton-transfer reaction. Note that the orientation of the dipole moment for both normal and tautomer species is arbitrarily picked.

Accordingly, as depicted in Scheme 1, the long-range polarization interactions may result in a solvent-induced barrier channeling into the proton-transfer reaction.

* Address correspondence to these authors. E-mail: chop@ntu.edu.tw and chenct@ntu.edu.tw.

10.1021/jp048415k CCC: $27.50
Published on Web 07/03/2004

SCHEME 2: Molecular Structures of Various Compounds Studied

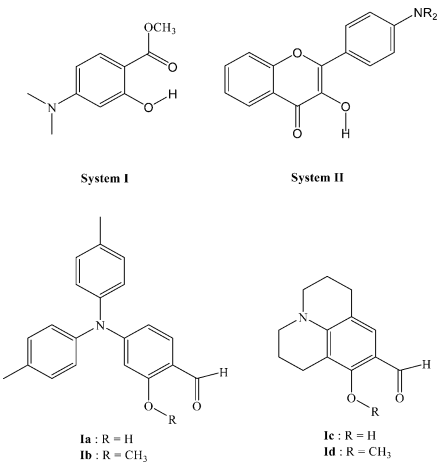

However, cases regarding solvent dipolar relaxation coupled ESIPT are rare because the dipolar change during ESIPT is, in general, not as significant as that in the case of the electron transfer, unless the Franck−Condon excited state undergoes gigantic dipolar changes due to, for example, a charge-transfer effect. In one approach, the design of such a system can be accomplished by incorporating an electron-donating or -accepting moiety into the chromophore, while the intramolecular hydrogen bond remains intact, so that a electron/proton transfer coupled reaction may take place in the excited state. Seminal studies on molecules exhibiting remarkable solvent polarization dependent ESIPT reaction dynamics should be ascribed to two prototypical systems, namely *p*-*N*,*N*-(dimethylamino)methylsalicylate (**I**)[8] and 4′-*N*,*N*-dialkylamino-3-hydroxyflavones (**II**) (see Scheme 2).[9−11] In polar, aprotic solvents, in contrast to a dominant tautomer emission resulting from ultrafast ESIPT in their corresponding parent molecules, i.e., methylsalicylate and 3-hydroxyflavone, multiple and dual emissions were observed in systems **I** and **II**, respectively. For system **I**, steady state and picosecond transient absorption measurements aimed at the characterization of multiple emissions have been reported,[8b] while detailed solvation coupled ESIPT dynamics have not yet been explored. For system **II**, applying the Marcus electron-transfer model and picosecond time-resolved study, Kelley and co-workers[10] were able to describe the overall reaction dynamics through a combination of solvent polarity and proton-transfer reaction coordinates, in which the proton-tunneling rate is concluded to be relatively much slower than the rate of solvent relaxation. Thus, a nonadiabatic type of proton transfer takes place essentially after solvent equilibration is established in the excited state.

For both systems, limited by the temporal resolution, any faster components of <10 ps were not resolvable in previous studies. It is thus crucial to extend the investigation of relevant systems toward the faster time domain to gain further insights into the solvent polarity coupled ESIPT dynamics. Two key issues to be explained include (1) the intrinsic ESIPT dynamics for those charge/proton-transfer coupled systems in nonpolar solvents such as cyclohexane, where the perturbation is minimized, and (2) more rigorous investigation into the solvation dynamics coupled ESIPT reaction, such as the differentiation among solvent relaxation, proton-transfer dynamics, vibrational cooling process, etc. on these systems. We believe that these issues can be probed through femtosecond dynamic approaches with the assistance of steady-state measurements. To achieve these goals, 2-hydroxy-4-(di-*p*-tolylamino)benzaldehyde (**Ia**, see Scheme 2) was designed and synthesized. **Ia** is superior to the aforementioned systems, i.e., **I** and **II**, based on several advantages. First of all, unlike 3-hydroxyflavone derivatives (i.e. system **II**), which are subject to the photolysis reaction on the pyrone ring,[12] **Ia** and corresponding analogues **(Ib−d)** are much more photoresistant (vide infra). This is particularly important in the fluorescence upconversion measurement, where the degradation commonly takes place through multiphoton events, resulting in experimental difficulties and/or artifacts. Second, the existence of different hydrogen bonding conformers (e.g. O−H- - -O═C and O−H- - -OCH_3 sites) for system **I** in the ground state complicates the spectral and dynamic assignments. Conversely, the lack of a $-OCH_3$ functional group ensures the existence of only one HB (O−H- - -O═C) conformer in **Ia**, simplifying both spectroscopic and dynamical approaches. Moreover, in contrast to system **I**, introducing the di-*p*-tolyl amino substituent to **Ia** pushes the spectral red shift of the $S_0 \rightarrow S_1$ ($\pi\pi^*$) transition toward 380−420 nm, which is in the optimal output range of our current femtosecond laser system.

The following sections are organized according to a sequence of steps in which after the experimental expression, we first performed detailed solvent-dependent absorption and emission experiments to determine their steady-state spectral properties. Subsequently, the dynamics of reaction/relaxation of **Ia** and its corresponding derivatives are investigated and discussed on the basis of femtosecond time-resolved studies under various solvent polarities. Finally, a plausible proton/charge-transfer mechanism is proposed to describe the overall reaction dynamics through a combination of solvent polarity and proton-transfer reaction coordinates.

2. Experimental Section

2.1. General Information. All reactions were performed under nitrogen. Solvents were distilled from appropriate drying agents prior to use. Commercially available reagents were used without further purification unless otherwise stated. All reactions were monitored by TLC with Merck precoated glass plates (0.20 mm with fluorescent indicator UV_{254}) and were visualized with UV light irradiation at 254 nm. Flash column chromatography was carried out with use of silica gel from Merck (230−400 mesh). Mass spectra were obtained on a JEOL SX-102A instrument operating in electron impact (EI) or fast atom bombardment (FAB) mode. The ^{1}H and ^{13}C NMR spectra were obtained on Bruker spectrometers operating at frequencies as indicated for each compound. Chemical shifts were reported relative to $CDCl_3$ (δ_H 7.24) and at 77.0 ppm in $CDCl_3$ [δ_C (central line of t)]. FT-IR spectra were recorded on a Nicolet magna-IR 550 series II. Melting points were uncorrected.

2.2. Materials. 9-Formyl-8-hydroxyjulolidine **(Ic**, Aldrich) was twice recrystallized from CH_2Cl_2. The purity was checked by corresponding ^{1}H NMR and fluorescence excitation spectra.

(3-Methoxyphenyl)di-p-tolylamine (1). A mixture of 3-methoxyaniline (1.24 g, 10 mmol), 4-iodotoluene (5.45 g, 25 mmol), copper bronze powder (1.92 g, 30 mmol), 18-crown-6 (0.52 g, 2 mmol), anhydrous potassium carbonate (4.83 g, 35 mmol), and 1,2-dichlorobenzene (30 mL) was stirred and refluxed for 96 h. After cooling, the insoluble inorganic material was filtered off and rinsed with CH_2Cl_2 a few times. The combined filtrates were concentrated under reduced pressure, and the resulting residue was purified by flash column chromatography on silica gel eluted with hexane/CH_2Cl_2 (10:1) to yield the desired product as a blonde oil (2.33 g, 77%). TLC (CH_2Cl_2/hexane,

1:10, v/v) R_f 0.3; ^{1}H NMR (400 MHz, $CDCl_3$) δ 7.09 (t, J = 8.1 Hz, 1H), 7.05 (d, J = 8.5 Hz, 4H), 6.99 (d, J = 8.5 Hz, 4H), 6.60−6.56 (m, 2H), 6.48 (dd, J = 8.1,2.4 Hz, 1H), 3.69 (s, 3H), 2.30 (s, 6H); ^{13}C NMR (100 MHz, $CDCl_3$) δ 160.33, 149.55, 145.26, 132.47, 129.79, 129.55, 124.72, 115.21, 108.48, 106.90, 55.16, 20.77; FAB-MS *m/z* 303.2 (M^+), FAB-HRMS for $C_{21}H_{21}NO$ calcd 303.1623, found 303.1631; FT-IR (neat) 2998.9, 2919.3, 1597.8, 1448.6 cm^{-1}.

*2-Methoxy-4-(di-p-tolylamino)benzaldehyde (**Ib**).* To a solution of $POCl_3$ (0.3 mL, 3.3 mmol) in 2 mL of DMF, which had been stirred for 30 min at 0 °C for 30 min, was added compound **1** (0.91 g, 3.0 mmol) dissolved in 5 mL of dry DMF dropwise at 0 °C. After being stirred an hour at 0 °C, the reaction was slowly warmed to room temperature and then heated to 70 °C for 6 h. The reaction was cooled to room temperature and quenched with water. The mixture was extracted with CH_2Cl_2. Combined organic layers were dried over $MgSO_4$, filtered, and concentrated under reduced pressure. The residue was purified by flash column chromatography on silica gel eluted with EtOAc/hexane (1:10) to give a yellowish solid **Ib** (0.70 g, 70%). Mp 103−105 °C; TLC (EtOAc/hexane, 1:10, v/v) R_f 0.3; ^{1}H NMR (400 MHz, $CDCl_3$) δ 10.17 (s, 1H), 7.60 (d, J = 8.7 Hz, 1H), 7.12 (d, J = 8.4 Hz, 4H), 7.05 (d, J = 8.4 Hz, 4H), 6.43 (dd, J = 8.7,2.0 Hz, 1H), 6.36 (d, J = 2.0 Hz, 1H), 3.66 (s, 3H), 2.32 (s, 6H); ^{13}C NMR (100 MHz, $CDCl_3$) δ 187.67, 163.14, 155.14, 143.36, 135.04, 130.24, 129.84, 126.48, 117.46, 111.15, 100.42, 55.33, 20.93; FAB-MS *m/z* 331.1 (M^+), FAB-HRMS for $C_{22}H_{21}NO_2$ calcd 331.1572, found 331.1569; FT-IR (neat) 2860.5, 2765.9, 1672.8, 1617.8, 1338.8 cm^{-1}. Anal. Calcd for $C_{22}H_{21}NO_2$: C, 79.73; H, 6.39; N, 4.23. Found: C, 79.69; H, 6.48; N, 4.05.

*2-Hydroxy-4-(di-p-tolylamino)benzaldehyde (**Ia**).* A solution of boron tribromide (0.2 mL, 2.1 mmol) in 5 mL of dry CH_2Cl_2 was added dropwise to a solution of compound **Ib** (0.33 g, 1.0 mmol) in 20 mL of dry CH_2Cl_2 at −78 °C over 20 min. The solution was stirred at −78 °C for an additional 2 h and then at room temperature. After the mixture was stirred for 20 h at room temperature, water was added carefully to consume excess boron tribromide. The acidic aqueous solution was extracted with CH_2Cl_2 (50 mL × 3), and the combined organic layers were dried over $MgSO_4$ and concentrated under reduced pressure. The greenish residue was purified by flash column chromatography eluted with EtOAc/hexane (1:10) to yield a yellowish solid (0.24 g, 75%). Mp 133−135 °C; TLC (EtOAc/hexane, 1:10) R_f 0.40 (EtOAc/hexane, 1:10); ^{1}H NMR (400 MHz, $CDCl_3$) δ 11.40 (s, 1H), 9.54 (s, 1H), 7.22 (d, J = 8.7 Hz, 1H), 7.14 (d, J = 8.4 Hz, 4H), 7.06 (d, J = 8.4 Hz, 4H), 6.39 (dd, J = 8.7, 2.2 Hz, 1H), 6.26 (d, J = 2.2 Hz, 1H), 2.33 (s, 6H); ^{13}C NMR (100 MHz, $CDCl_3$) δ 192.89, 163.61, 155.71, 142.78, 135.68, 134.58, 130.35, 126.92, 113.86, 110.01, 103.71, 20.95; FAB-MS *m/z* 317.1 (M^+), FAB-HRMS for $C_{21}H_{19}NO_2$ calcd 317.1416, found 317.1385; FT-IR (neat) 3025.4 (br), 2919.3, 1631.3, 1609.4, 1498.9 cm^{-1}. Anal. Calcd for $C_{21}H_{19}NO_2$: C, 79.47; H, 6.03; N, 4.41. Found: C, 79.21; H, 6.02; N, 4.40.

*9-Methoxy-2,3,6,7-tetrahydro-1H,5H-pyrido[3,2,1-ij]quinoline-8-carbaldehyde (**Id**).* To a suspension of NaH (60% in oil, 176 mg, 2.6 mmol) in THF (20 mL) was added slowly **Ic** (500 mg, 2.2 mmol) at 0 °C. After the mixture was stirred for 30 min, methyl iodide (369 mg, 2.6 mmol) under nitrogen (25 °C) was added and the solution was subjected to heat at 60 °C for 12 h. The mixture was then cooled to room temperature followed by the addition of water to consume unreacted NaH. The organic solvent was removed via reduced pressure and the resulting residue was then extracted with CH_2Cl_2. The combined organic layers were dried with $MgSO_4$ and filtered, and the solvent was removed by a rotary evaporator. The residue was purified by flash column chromatography eluted with EtOAc/hexane (1:10 v/v), yielding the desired product (1.9 g, 89%). ^{1}H NMR ($CDCl_3$, 400 MHz) δ 9.98 (1 H, s), 7.32 (1 H, s), 3.8 (3H, s), 3.26 (t, J = 7.6 Hz, 4H), 2.72 (4 H, m), 1.93 (qu, J = 6.0 Hz, 4 H); FAB-MS *m/z* (rel intensity) 231 (M^+, 100%).

2.3. Photospectroscopic Measurements. Steady-state absorption and emission spectra were recorded by a Hitachi (U-3310) spectrophotometer and an Edinburgh (FS920) fluorimeter, respectively. The various solvents were of spectragrade quality (Merck Inc.) and were used right after being received. Benzene and acetonitrile showed traces of fluorescence impurities and were fractionally distilled prior to use.

Nanosecond lifetime studies were performed with an Edinburgh FL 900 photon-counting system with a hydrogen-filled/or a nitrogen lamp as the excitation source. The emission decays were analyzed by the sum of exponential functions, which allows partial removal of the instrument time broadening and consequently renders a temporal resolution of ∼200 ps. The setup of picosecond dynamical measurements consists of a femtosecond Ti−Sapphire oscillator (82 MHz, Spectra Physics).[13] The fundamental train of pulses was pulse-selected (Neos, model N17389) to reduce its repetition rate to typically 0.8−8 MHz, and then used to produce second harmonics (375−425 nm) as an excitation light source. A polarizer was placed in the emission path to ensure that the polarization of the fluorescence was set at the magic angle (54.7°) with respect to that of the pump laser to eliminate the fluorescence anisotropy. An Edinburgh OB 900-L time-correlated single photon counting system was used as a detecting system, rendering a temporal resolution of ∼15 ps. The fluorescence upconversion measurements were performed with a femtosecond optically gated system (FOG-100, CDP). The fundamental of a Ti:sapphire laser (Spectra Physics) at 750−850 nm with an average power of 0.5 W and a repetition rate of 82 MHz was used to produce second harmonics (SH) at 375−425 nm by focusing onto a 0.5 mm thick BBO type-I crystal. The SH was then separated from the fundamental pulses with a dichroic mirror and used as pump pulses. The pump pulses were focused onto a rotating cell, and the optical pathlength was 1.0 mm. The resulting fluorescence was collected by an achromatic lens and then focused on another BBO type-I crystal (0.5 mm). The optical delayed remaining fundamental pulses were also focused on the BBO crystal and used as gate pulses for the sum-frequency generation. A Berek's variable waveplate was placed in the pump beam path to ensure that the polarization of the pump laser was set at the magic angle (54.7°) with respect to that of the probe laser to eliminate the fluorescence anisotropy. The upconverted signal was then separated by an F/4.9 (f = 380 mm) single monochromator (CDP2022) and detected via a photon counting PMT (R1527P, Hamamatsu). The cross correlation between SH and the fundamental had a full width at half-maximum (fwhm) of ∼150 fs, which was chosen as a response function of the system.

2.4. Computational Approaches. The Gaussian 98 program[14] was used to perform the ab initio calculation on the molecular structure. Geometry optimizations for all structures were carried out with the 6-31G(d′,p′) basis set at the Hartree−Fock (HF) level. Hessians and hence vibrational frequencies were also performed to check whether the optimized geometrical structure for those molecules is at an energy minimum, transition state, or higher order saddle point.

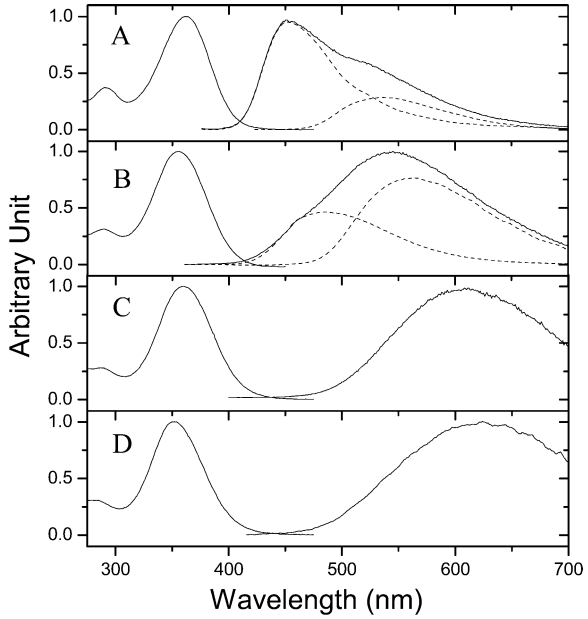

Figure 1. Static absorption and fluorescence spectra of **Ia** in (A) cyclohexane, (B) benzene, (C) dichloromethane, and (D) acetonitrile at 298 K. Dashed curves express the spectra fit for **Ia** in cyclohexane.

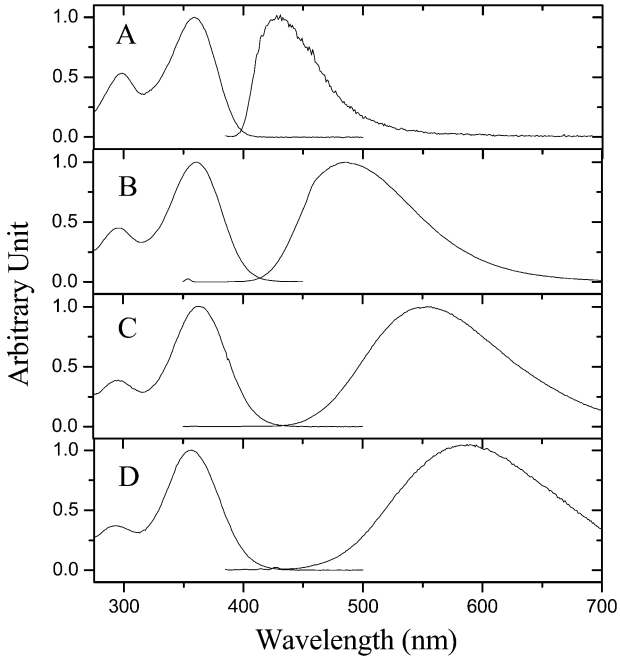

Figure 2. Static absorption and fluorescence spectra of **Ib** in (A) cyclohexane, (B) benzene, (C) dichloromethane, and (D) acetonitrile at 298 K.

3. Results

3.1. Steady-State Approach. In cyclohexane, **Ia** exhibits the lowest singlet $S_0 \rightarrow S_1$ ($\pi\pi^*$) absorption band maximum at 365 nm (see Figure 1A, $\epsilon_{365} \sim 1.110^4$ M^{-1} cm^{-1}). The spectral feature resembles that of **Ib** (see Figure 2A), generally treated as a nonintramolecular hydrogen bond (HB) and hence a non-ESIPT model due to the lack of the O−H proton. In contrast to 2-hydroxybenzaldehyde (**2HBA**), in which the absorption maximum could be bathochromically shifted to as large as 15 nm with respect to 2-methoxybenzaldehyde due to the intramolecular HB enhancing π electrons delocalization,[15] the spectral shift on the $S_0 \rightarrow S_1$ peak wavelength between **Ia** and **Ib** was negligibly small (<3 nm, see Figures 1 and 2 for comparison). Upon increasing the solvent polarity, a blue shift of the absorption maximum was observed for **Ia** from 365 (cyclohexane) to 358 nm (CH_3CN, see Figure 1D). In view of the low ionization energy for the di-*p*-tolyl amino substituents, these results can plausibly be rationalized by the manifestation of the $S_0 \rightarrow S_1$ absorption band in **Ia** and **Ib** by a charge-transfer character incorporating ditolylamine (electron donor) and carbonyl oxygen (electron acceptor). The dominant charge-transfer property suppresses the π electrons delocalization induced by HB, resulting in a negligible difference in absorption peak wavelength between **Ia** and **Ib**. Franck−Condon excitation causes significant dipolar changes on **Ia** (or **Ib**), and hence the unfavorable solvated configuration in the excited state, rationalizing the hypsochromic shifts of the absorption spectrum upon increasing solvent polarity.

The emission of **Ia** in cyclohexane consists of dual bands maximized at 450 and ∼530 nm (shoulder, see Figure 1A). The ratio for the 450 nm versus 530 nm emission intensity reveals concentration independence, eliminating the emission associated with any high-order aggregation. The entire dual emission originating from a common ground-state species is ascertained by the same fluorescence excitation spectra throughout the monitored wavelengths of 420−650 nm, which are also effectively identical with the absorption spectrum, indicating that the entire emission results from a common Franck−Condon excited state. In a comparative study, **Ib** exhibited a single emission maximized at ∼435 nm in cyclohexane, while the 530-nm band apparently disappeared (see Figure 2A). The difference in structures between **Ia** and **Ib** mainly lies in the lack of intramolecular HB in **Ib**. Furthermore, **2HBA**, a well-known ESIPT model, exhibits a unique 520-nm proton-transfer tautomer emission.[15] Thus, it is reasonable to ascribe the 530-nm band in **Ia** to the tautomer emission resulting from ESIPT. The 450-nm emission was accordingly assigned to the normal (i.e. nonproton-transfer) emission. Similarly, the entire emission of **Ia** in benzene originating from the same Franck Condon excited state is ascertained by the identical excitation spectra (not shown here). However, since the emission full width at half-maximum (fwhm) is wider than that of **Ib**, the existence of dual emissions in **Ia** is also possible (see Figures 1B and 2B for comparison), which unfortunately could not be resolved due to the strong spectral overlap (vide infra).

In contrast to the occurrence of ultrafast ESIPT in **2HBA**,[16] giving rise to an exclusive ∼520 nm tautomer emission, the appearance of dual emissions for **Ia** in nonpolar solvents, in which the normal fluorescence dominates in cyclohexane, is remarkable. Because there are no other HB conformers existing for **Ia** in the ground state, the steady state result simply implies the existence of either an appreciable barrier or an excited-state equilibrium associated with ESIPT. Further insights into the reaction dynamics will be gained via the femtosecond fluorescence upconversion study.

As shown in Figure 1, in contrast to the appearance of dual emissions in **Ia** in cyclohexane, the steady-state approach revealed a broad, single-fluorescence band in all polar, aprotic solvents studied. Furthermore, despite the blue shift in the absorption profile, the fluorescence peak frequency exhibited drastic solvent dependence, being decreased as the solvent polarity increased. The results support the operation of excited-state charge transfer, yielding a gigantic change in the dipole moment. Perhaps the strongest support for this viewpoint is given by the nonproton-transfer model **Ib**, which revealed similar solvent-polarity dependence in the peak maximum, being red shifted from 435 nm in cyclohexane to 580 nm in CH_3CN (see Figure 2). Further structural verification of the charge-

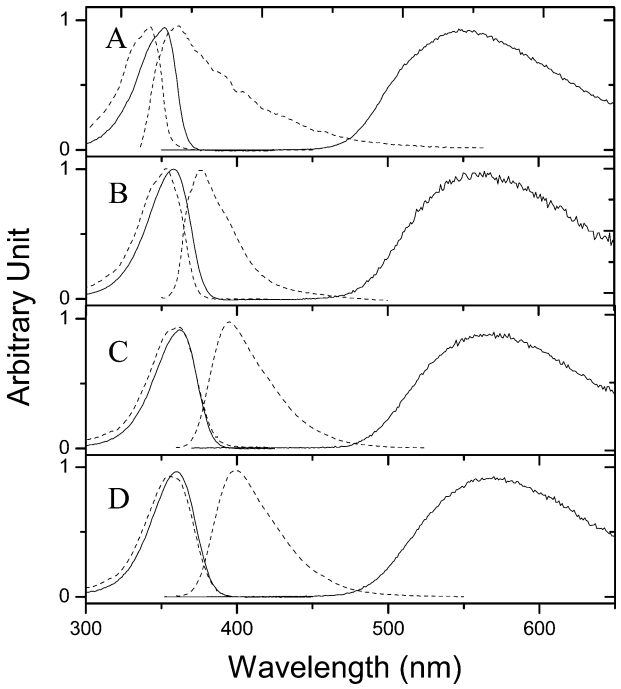

Figure 3. Static absorption and fluorescence spectra of **Ic** (—) and **Id** (- - -) in (A) cyclohexane, (B) benzene, (C) dichloromethane, and (D) acetonitrile at 298 K.

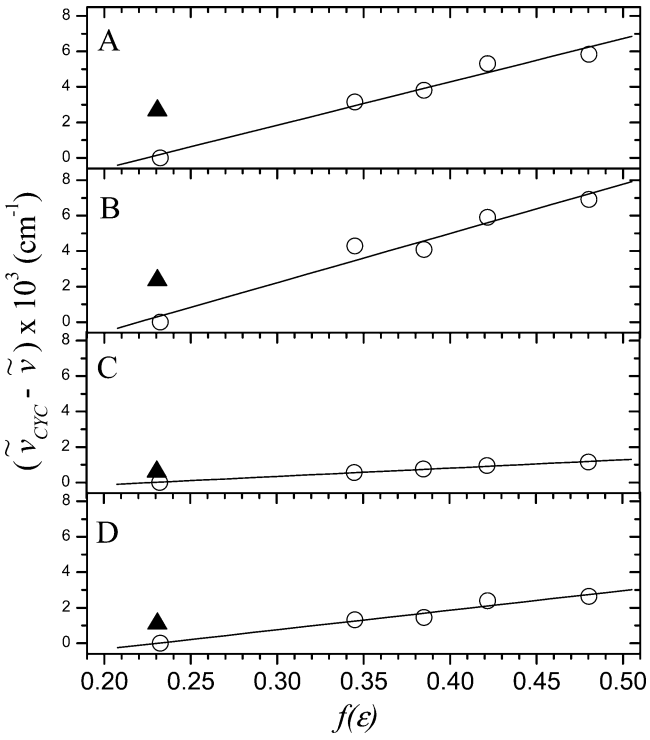

Figure 4. The plot of fluorescence maximum frequencies for (A) **Ia**, (B) **Ib**, (C) **Ic**, and (D) **Id** as a function of solvent polarity parameter $f(\epsilon)$: ○, data for cyclohexane, ethyl ether, ethyl acetate, dichloromethane, and acetonitrile; ▲, data for benzene.

transfer emission is given by **Ic** and **Id** (see Scheme 2), in which the nitrogen lone pair electrons are locked, to a certain extent, in an unfavorable orientation so that the charge transfer efficiency may be largely inhibited. Figure 3 depicts the emission of **Id** in various solvents, in which the emission peak is only slightly red shifted from 375 nm in cyclohexane to 400 nm in CH_3CN, supporting the proposed charge-transfer mechanism incorporated diarylamino nitrogen in **Ib**. Conversely, as shown in Figure 3, **Ic** revealed a large Stokes shifted, solvent-polarity independent ~520 nm emission band. Obviously, under the diminution of excited-state charge transfer, ESIPT is decoupled from the solvent perturbation. Accordingly, **Ic** is expected to exhibit similar photophysical properties as **2HBA**, i.e., fast ESIPT reaction, resulting in a proton-transfer tautomer emission. To simplify a further approach, the emission spectra of **Ib** and **Ic** can thus be used to simulate the normal (i.e. charge transfer) and tautomer emission profiles, respectively, of **Ia**. As shown in the dotted-line curve of Figure 1, the overall emission spectrum of **Ia** in cyclohexane is well fitted by the combination of **Ib** and **Ic**, further supporting the dual emission properties for **Ia** in cyclohexane.

The solvent-polarity dependent emission property can be specified quantitatively according to the theory derived from dielectric polarization, specifying that the spectral shifts of the fluorescence upon increasing the solvent polarity depend on the difference in permanent dipole moments between ground and excited states. The magnitude of the excited-state dipole moments can thus be estimated by a method incorporating the fluorescence solvatochromic shift.[17−21] If the dipole moments of the solute are approximated by a point dipole in the center of a spherical cavity with a radius a_0, on the basis of small solvent dependent absorption properties and negligence of the solute polarizability, one obtains

$$\tilde{\nu}_f = \tilde{\nu}_f^{vac} - \frac{2(\vec{\mu}_e - \vec{\mu}_g)^2}{hca_0^3}\Delta f \qquad \text{(I)}$$

where $\tilde{\nu}_f$ and $\tilde{\nu}_f^{vac}$ in eq I are the spectral position (in terms of wavenumber) of the solvation equilibrated fluorescence maxima and the value extrapolated to the diluted gas phase, respectively, $\vec{\mu}_g$ and $\vec{\mu}_e$ are the dipole moment vectors of the ground and excited states, and Δf is the solvent polarity parameter function and is generally expressed as $\Delta f = (\epsilon - 1)/(2\epsilon + 1)$, where ϵ denotes the static dielectric constant of the solvent. The plot of fluorescence peak frequency as a function of Δf is shown in Figure 4, parts A and B, for **Ia** and **Ib**, respectively. As predicted by eq I, a linear relationship is found from ethyl ether to acetonitrile, and slopes as steep as $-2.44\ 10^4$ and $-2.78\ 10^4$ cm^{-1} were obtained for **Ia** and **Ib**, respectively, consistent with its assignment of the charge-transfer emission. a_0 in eq I was estimated to be 6.55 Å for both **Ia** and **Ib** via the Hartree−Fock method with 6-31G(d′,p′) basis sets. Accordingly, the change in dipole moment between ground and excited states was deduced to be as large as 27 and 28 D for **Ia** and **Ib**, respectively. Moreover, the proton-transfer tautomer emission of **Ic** can be clearly distinguished by its rather small polarity dependence in the Lippert's plot (see Figure 4C).

3.2. Femtosecond Time-Resolved Spectroscopy. *3.2.1. Femtosecond Dynamics of Nonproton-Transfer Cases.* To make a clear differentiation between charge transfer and proton transfer, we would first like to present the relaxation dynamics of the nonproton-transfer case **Ib**. The time-resolved fluorescence of **Ib** in cyclohexane is straightforward, and it was established by a response-limited (<130 fs) rise and a single-exponential decay component ($\tau_f \sim 70$ ps, see Figure 5) at any monitored wavelengths. The fast decay rate correlates well with its rather small quantum yield of $\sim 1.2 \times 10^{-3}$ measured in cyclohexane. Due to the appreciable triplet−triplet absorption (λ_{max} at 480 and 560 nm) and intensive phosphorescence in a 77 K methylcyclohexane glass (not shown here), it is plausible that similar to *o*-methoxybenzaldehyde,[3a] the lowest singlet excited state of **Ib** in cyclohexane is in an $^1n\pi^*$ configuration.

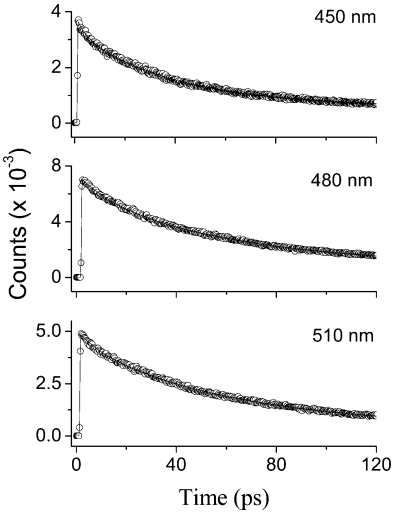

Figure 5. Time-resolved sum frequency signal of fluorescence and gate pulse (800 nm) for **Ib** in cyclohexane. The solid lines express the corresponding best-fitted curves.

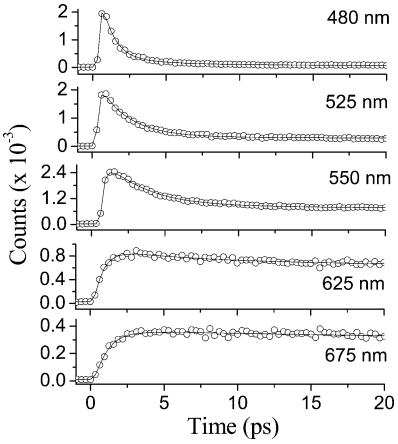

Figure 6. Time-resolved sum frequency signal of fluorescence and gate pulse (800 nm) for **Ib** in dichloromethane. The solid lines express the corresponding best-fitted curves.

The proximity in energetics between $S_{\pi\pi^*}$ and $S_{n\pi^*}$ manifolds may cause significant state mixing, resulting in the fluorescence relaxation dynamics dominated by the rate of $^1n\pi^* \rightarrow {}^3\pi\pi^*$ intersystem crossing.

Figures 6 and 7 show the time-resolved fluorescence spectra of **Ib** in dichloromethane and acetonitrile, respectively. Similar trends were observed in both solvents, in which the emission dynamics are nonsingly exponential. Detailed fitting parameters for both early-time relaxation dynamics and population decay rate are listed in Table 1. Upon monitoring at shorter emission wavelengths, the relaxation dynamics consist of an ultrafast rise (<130 fs), a fast, resolvable (~100 fs to a few ps) decay, and rather long (>1 ns) decay components. The decay components require at least two, and for some wavelengths even three, exponential terms to achieve good convoluted fits for **Ib**. The >1-ns decay component, measured by the pico-nanosecond single photon counting technique, was resolved to be 3.7 and 1.1 ns in CH_2Cl_2 and CH_3CN, respectively, and was then attributed to the population decay (radiative plus nonradiative) of the solvent-equilibrated S_1 state. Upon increasing the monitored wavelength, while the population decay remains unchanged, the decay time of the early (fast) components gradually increases, accompanied by a decrease in the magnitude, and finally becomes a rise component at the emission tail. Two remarks can be made according to the data analyses. First,

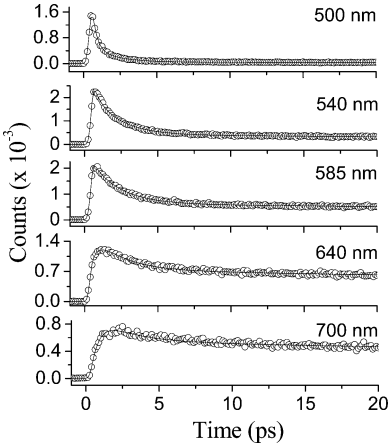

Figure 7. Time-resolved sum frequency signal of fluorescence and gate pulse (800 nm) for **Ib** in acetonitrile. The solid lines express the corresponding best-fitted curves.

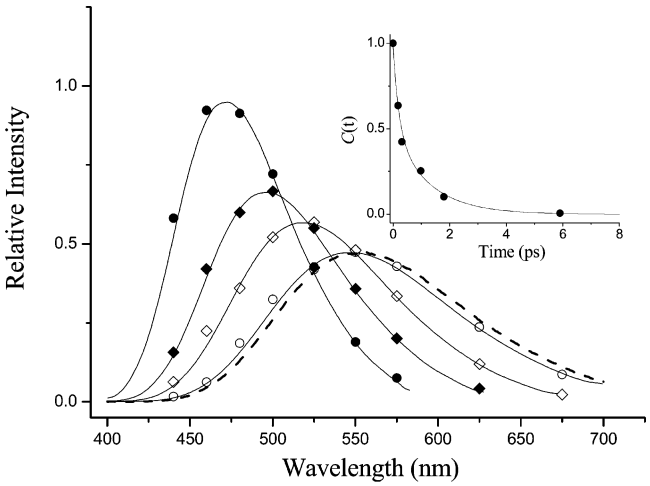

Figure 8. The temporal emission spectra of **Ib** in CH_2Cl_2 acquired at a delay time of (●) 0.25, (◆) 0.5, (◇) 1.0, and (○) 3.0 ps. The dashed line indicates the steady-state fluorescence. The solid lines express the fitted curves. Insert: The plot of $C(t)$ versus the delay time in CH_2Cl_2. $C(t)$ is defined in the text.

the best-fitted time constants for the fast decay (or rise) components vary by the probed emission wavelengths. Second, as shown in Figure 8, the temporal spectral evolution of the emission in, e.g., CH_2Cl_2 reveals a continuous spectral shift in fluorescence peak maxima. If the large Stokes shift results from the interconversion of two electronically excited states, i.e., a locally excited and a charge transfer species, two distinct fluorescence bands should appear during the time-dependent spectral evolution, and the time constants should be independent of the monitored wavelengths. We thus ascribe the early time evolution of **Ib** in dipolar solvents to a continuously evolving solvent relaxation rather than an interconversion between two excited species. On the basis of the time-resolved Stokes shifted model,[22] the solvation relaxation time τ_s can be extracted from the experimental function expressed as

$$C(t) = \frac{\upsilon(t) - \upsilon(\infty)}{\upsilon(0) - \upsilon(\infty)} \qquad \text{(II)}$$

where $\upsilon(0)$, $\upsilon(\infty)$, and $\upsilon(t)$ denote frequency maxima of the upconverted fluorescence probed at $t = 0$, ∞, and intermediate times t, respectively. The plot of $C(t)$ versus delay time in CH_2Cl_2 shown in the insert of Figure 8 reveals a dual exponential decay-like profile, and a mean τ_s[23] was estimated to be 0.75

TABLE 1: The Photophysical Properties of Ia and Ib in Various Solvents

	solvent	emission (Φ)	early dynamics[a]	population decay[b]
Ia	CHE	450 nm (1.6×10^{-2})	450 nm [τ_1: 0.37 (0.123)]	0.36 (0.042[c])
			488 nm [τ_1: 0.35 (0.096)]	
	BEN	550 nm (1.1×10^{-1})	460 nm [τ_1: 0.31 (0.02); τ_2: 3.2 (4.5×10^{-3})]	
			485 nm [τ_1: 2.81(0.08); τ_2: 12.1 (0.13)]	
			525 nm [τ_1: 4.11 (6×10^{-3}); τ_2: 17.9 (0.015)]	2.0
			575 nm [τ_1: 0.17 (-0.27); τ_2: 14.6 (8×10^{-3})]	
			650 nm [τ_1: 0.32 (-6.9×10^{-3})]	
	DCM	575 nm (5.6×10^{-3})	500 nm [τ_1: 0.41 (6×10^{-3}); τ_2: 1.7 (8.5×10^{-3})]	
			565 nm [τ_1: 0.91 (4×10^{-3}); τ_2: 3.2 (6.5×10^{-3})]	
			680 nm [τ_1: 0.18 (-1.1×10^{-3}); τ_2: 4.1 (9×10^{-3})]	0.37
			720 nm [τ_1: 0.34 (-0.037); τ_2: 4.9 (9.5×10^{-3})]	
			750 nm [τ_1: 0.48 (-6×10^{-3}); τ_2: 3.9 (2.9×10^{-3})]	
	ACN	620 nm (1.0×10^{-3})	480 nm [τ_1: 0.21 (4×10^{-3})]	
			540 nm [τ_1: 0.51 (2.5×10^{-3})]	
			620 nm [τ_1: 0.92 (2.8×10^{-3}); τ_2: 3.3 (4.5×10^{-3})]	0.11
			670 nm [τ_1: 1.22 (1.5×10^{-3}); τ_2: 8.3 (4.4×10^{-4})]	
			720 nm [τ_1: 1.55 (3.6×10^{-4}); τ_2: 11.7 (2.2×10^{-4})]	
Ib	CHE	435 nm (1.2×10^{-3})		0.07
	BEN	490 nm (1.1×10^{-1})	440 nm [τ_1: 2.51 (0.093)]	
			460 nm [τ_1: 3.9 (0.35)]	
			488 nm [τ_1: 5.05 (0.14)]	
			510 nm [τ_1: 1.65 (-0.2); τ_2: 4.7 (0.16)]	5.2
			560 nm [τ_1: 2.11 (-0.18)]	
			650 nm [τ_1: 2.47 (-0.042)]	
	DCM	555 nm (2.2×10^{-1})	480 nm [τ_1: 0.76 (0.14); τ_2: 3.1 (0.32)]	
			525 nm [τ_1: 0.75 (0.11); τ_2: 3.8 (0.25)]	
			550 nm [τ_1: 0.23 (-0.086); τ_2: 3.0 (0.19)]	3.7
			625 nm [τ_1: 0.59 (-0.098); τ_2: 2.9 (0.11)]	
			675 nm [τ_1: 0.85 (-0.02)]	
	ACN	580 nm (4.2×10^{-2})	500 nm [τ_1: 0.39 (4.5×10^{-3}); τ_2: 1.54 (5.3×10^{-3})]	
			540 nm [τ_1: 0.41 (1.4×10^{-3}); τ_2: 1.80 (4.7×10^{-3})]	
			585 nm [τ_1: 0.45 (3.6×10^{-4}); τ_2: 1.98 (2.1×10^{-3})]	1.1
			640 nm [τ_1: 0.43 (-2.1×10^{-3}); τ_2: 2.08 (2.3×10^{-3})]	
			700 nm [τ_1: 0.55 (-2.6×10^{-3}); τ_2: 2.34 (1.1×10^{-3})]	

[a] In ps. Data listed in the early dynamics are the rise (negative preexponential factor) and short decay components. The much longer population decay components are not shown in this column. Data in parentheses are the fitted preexponential factors. [b] In ns. [c] Preexponential factor at 450 nm.

ps. Similar methods were applied for **Ib** in CH_3CN, and a τ_s of 0.42 ps was then extracted. Within the experimental error, the deduced τ_s of 0.75 in CH_2Cl_2 and 0.42 ps in CH_3CN is respectively in agreement with the average solvent relaxation time of 0.56 and 0.26 ps reported previously.[23]

It should be noted that the static spectroscopy and relaxation dynamics of **Ib** in benzene are quite different from those in cyclohexane. Despite the zero net dipole moment of benzene, the trend of time-dependent fluorescence in this solvent is more or less the same as those in dipolar solvents, consisting of wavelength-dependent short decay (or rise) components and a rather long population decay of 5.2 ns (see Figure 9). The τ_f of 5.2 ns with a corresponding quantum efficiency of 0.11 is drastically different from those in cyclohexane ($\tau_f = 70$ ps, $\Phi_f \sim 1.2 \times 10^{-3}$). The anomalous photophysical behavior in benzene is also revealed in the Lippert's plot (see Figure 4), in which the peak frequency versus $\Delta f(\epsilon)$ deviates considerably from others. The continuum dielectric models used in the Lippert's plot predict a similar emission peak frequency in both cyclohexane and benzene. Such models rely solely on the infinite wavelength dielectric properties of the solvent (ϵ_0 or $\epsilon(w)$) and thus cannot distinguish between truly nonpolar solvents (e.g. cyclohexane) and nondipolar solvents such as benzene. Benzene contains significantly easily polarized π electrons, which lead to large higher order multipole moments (quadrupole, octapole, etc.).[23,24] Thus, both the statics and dynamics of solvation in benzene are not qualitatively different from those in dipolar solvents. Equation I fails to convey usable information in the case of nondipolar solvents. However, just as in the case of the energetics, we expect the dynamics of solvation in nondipolar solvents to involve similar reorientational/translational solvent motions as in dipolar solvents, even if they are less readily modeled.[24] At this stage, simple theories to accurately model the solvation dynamics in benzene are not available. In addition, since the relevant approach is not a core issue in point, details will be elaborated elsewhere. Nevertheless, note that the fast decay monitored at, e.g., 440 nm (see Figure 9) is fitted to be

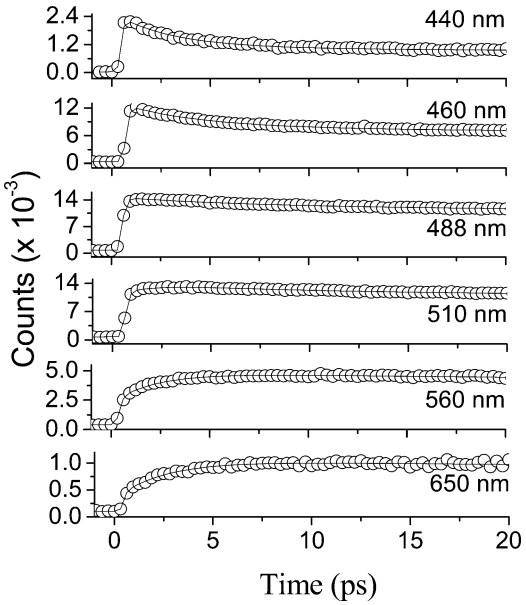

Figure 9. Time-resolved sum frequency signal of fluorescence and gate pulse (800 nm) for **Ib** in benzene. The solid lines express the corresponding best-fitted curves.

SCHEME 3: The Proposed Free Energy of the Solvated Ib as a Function of the Solvent Polarization[a]

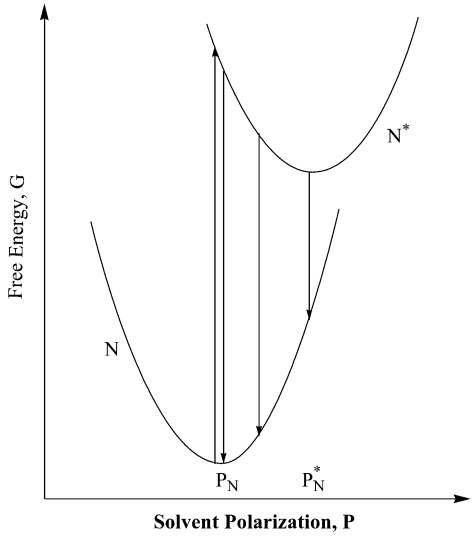

[a] P_N and P^*_N are the equilibrium polarization for the normal species in the ground and excited states, respectively.

2.5 ps, which is in the same magnitude as the average solvation time of 2.1 ps.[23]

In summary, upon electronic excitation, the dipolar change in **Ib** is quite large and can thus be treated as a charge transfer process. The coupling between locally excited and charge transfer states must be fairly strong so that the solvent polarization induced barrier is negligible. Under the absence of a reaction barrier, a common adiabatic solvation energetics of **Ib** is depicted in Scheme 3, where the nonequilibrium free energy (G) of the solute/solvent system for the ground state (S_0) and excited state (S_1) of **Ib** can be plotted as a function of an instantaneous solvent polarization P. Accordingly, the observed relaxation dynamics is mainly governed by the solvation process. Relative to cyclohexane, the much longer decay, and hence higher quantum yield, of **Ib** in benzene and dipolar solvents can be tentatively rationalized by the solvent stabilization of the $S_{\pi\pi}$* manifold, leading to the interconversion between $S_{\pi\pi}$* and $S_{n\pi}$* states so that the deactivation pathway dominated by the $S_{n\pi}$* $\rightarrow$ $T_{\pi\pi}$* intersystem crossing is drastically diminished.

3.2.2. Dynamics of Charge/Proton-Transfer Coupled Reaction. In comparison with **Ib**, the relaxation dynamics of **Ia** are relatively complicated due to the addition of one more reaction channel, namely the ESIPT pathway demonstrated by the steady-state emission measurements. In cyclohexane, the temporal resolution at the blue side, e.g. 450 nm, of the fluorescence (see Figure 10) consists of a response limited (<130 fs) rise component, a fast but resolvable decay of 0.37 ps, followed by a much slower decay that can be treated as an offset constant within an acquisition duration of 20 ps. While the decay time of 0.37 ps remains unchanged, the intensity ratio for the fast versus the slower decay component at $t \sim 0$ decreases with increases in the monitored emission wavelengths. The 0.37 ps decay component eventually disappears when the emission wavelength is monitored at, e.g., >560 nm, leading to a response limited rise and approximately constant decay components within 20 ps. Interestingly, despite the resolution of dual emission bands from the steady-state approach, the lifetime of the slow decay component, i.e., the population decay, acquired by the picosecond single photon counting method, was resolved to be 360 ps throughout the monitored dual emission of 420−700 nm. Note that although much of the normal and tautomer emissions overlap, according to the spectral fit in Figure 1, there is negligible overlap between normal (e.g. 420 nm) and tautomer (e.g. 680 nm) emissions, indicating that the identical population lifetime cannot be solely explained by the spectral overlap. The results lead us to conclude the establishment of an excited-state equilibrium between normal (i.e., charge transfer) and proton-transfer tautomer states, in which the rates of forward and reverse ESIPT are much faster than that of the population decay rate (i.e., k_1 and $k_{-1} \gg k_N + k_T$, see the following scheme) for both states. The ESIPT reaction scheme and its associated relaxation dynamics can be expressed as follows.

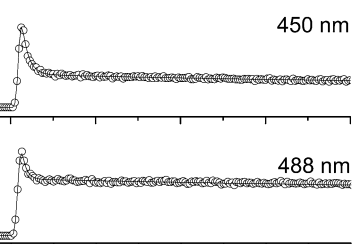

Figure 10. Time-resolved sum frequency signal of fluorescence and gate pulse (800 nm) for **Ia** in cyclohexane. The solid lines express the corresponding best-fitted curves.

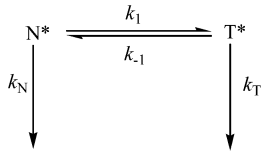

$$[N^*] = \frac{[N^*]_0}{\lambda_2 - \lambda_1}\{(\lambda_2 - X)e^{-\lambda_1 t} + (X - \lambda_1)e^{-\lambda_2 t}\} \quad (1)$$

$$[T^*] = \frac{k_1[N^*]_0}{\lambda_2 - \lambda_1}\{e^{-\lambda_1 t} - e^{-\lambda_2 t}\} \quad (2)$$

$$\lambda_1 \approx \frac{k_N + k_T K_{eq}}{1 + K_{eq}}, \qquad \lambda_2 = k_1 + k_{-1}$$

$$X = k_N + k_1, \qquad Y = k_T + k_{-1}$$

where k_1 and k_{-1} denote the forward and reverse rates of ESIPT, respectively. K_{eq} represents the equilibrium constant between N* and T* species. Accordingly, upon instantaneous population of N*, the excited normal species should undergo two decay pathways with time constants of λ_1 and λ_2, while the overall dynamics of the tautomer species should theoretically reveal rise and decay components with rate constants of λ_2 and λ_1, respectively. As shown in the dual spectral fit of the overall emission (see Figure 1A), the time-resolved normal emission monitored at <450 nm should be free from the interference of the tautomer emission. Thus, the resolved fast decay component

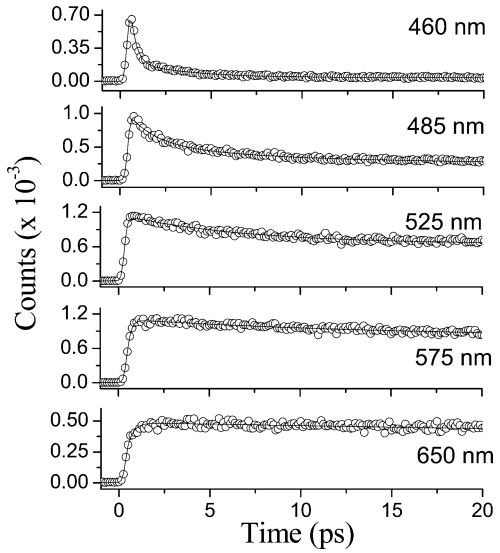

Figure 11. Time-resolved sum frequency signal of fluorescence and gate pulse (800 nm) for **Ia** in benzene. The solid lines express the corresponding best-fitted curves.

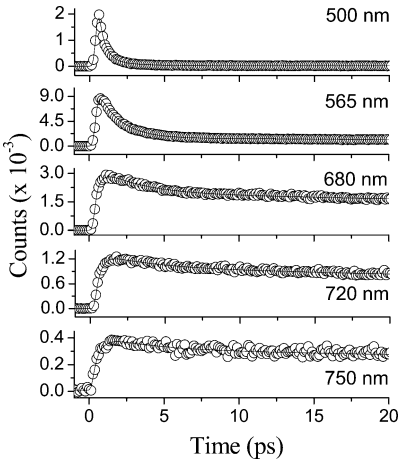

Figure 12. Time-resolved sum frequency signal of fluorescence and gate pulse (800 nm) for **Ia** in dichloromethane. The solid lines express the corresponding best-fitted curves.

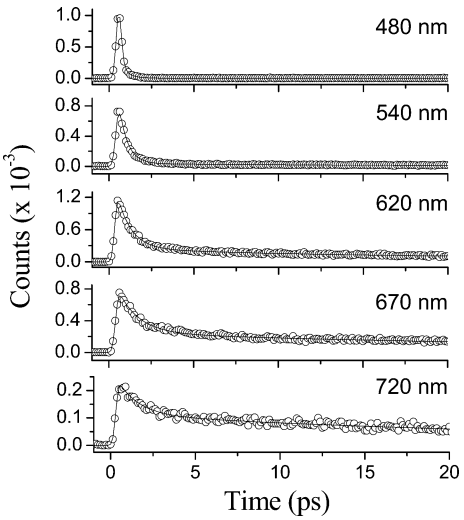

Figure 13. Time-resolved sum frequency signal of fluorescence and gate pulse (800 nm) for **Ia** in acetonitrile. The solid lines express the corresponding best-fitted curves.

with a rate constant of 370 fs^{-1} can be ascribed to the λ_2 ($=k_1 + k_{-1}$), and the decay rate of 360 ps^{-1} corresponds to the equilibrated population decay, i.e., λ_1. The preexponential factor for eq 1 can be further derived to

$$\frac{X - \lambda_1}{\lambda_2 - \lambda_1} \approx \frac{k_1}{k_1 + k_{-1}} \tag{3}$$

$$\frac{\lambda_2 - X}{\lambda_2 - \lambda_1} \approx \frac{k_{-1}}{k_1 + k_{-1}} \tag{4}$$

Thus, the ratio for (3) versus (4) is equivalent to $k_1/k_2 = K_{eq}$, which is also equal to the ratio of two exponential factors extracted experimentally (see Table 1). Accordingly, K_{eq} was deduced to be 2.94. Since $k_1 + k_{-1}$ was measured to be 2.7×10^{12} s^{-1}, k_1 and k_{-1} were then calculated to be 2.0×10^{12} and 6.8×10^{11} s^{-1}, respectively.

According to the precursor−successor type of kinetics described above, the upconverted signal monitored at the tautomer emission region should give rise to a rise and a decay component. In contrast, however, only a population decay rate constant λ_1 of 0.36 ns could be resolved upon monitoring at >550 nm. The results can be tentatively rationalized by the fact that the tautomer emission spectrum overlaps considerably with the normal species (see Figure 1A). As a result, the magnitude of the rise component of the tautomer emission is largely canceled out by the decay component of the normal emission. We have also made attempts to extract the thermodynamics between N* and T* species. In a temperature-dependent steady-state approach for **Ia** in methylcyclohexane, the overall emission intensity increased upon a decrease in the temperature. However, the intensity ratio for the 530 nm versus 450 nm band remained nearly unchanged from 330 to 160 K. Assuming a negligible ESIPT barrier and a similar temperature-dependent nonradiative decay rate, we thus tentatively propose an accidental degeneracy between N* and T* for the case of **Ia** in cyclohexane. Due to its charge-transfer property, any subsequent increase of the solvent polarity should further stabilize the normal (i.e., charge-transfer) state, resulting in a breakdown of the degeneracy described as follows.

Figures 11−13 depict the time-resolved spectra of **Ia** in benzene, dichloromethane, and acetonitrile, respectively. Detailed fitting parameters for early-time relaxation dynamics and population decay rate are listed in Table 1. Although both **Ia** and **Ib** seem to reveal similar steady-state spectral features in these solvents (see Figures 1 and 2 for comparison), drastically different relaxation dynamics between **Ia** and **Ib** were resolved. Because a similar trend in the differences was observed in these solvents, the results shown in Figures 11−13 can be discussed concurrently. In comparison with the relaxation dynamics of **Ib** in the same solvent, two remarks can be promptly pointed out for **Ia**. First of all, under identical experimental conditions, i.e., the same excitation frequency, intensity, and detecting parameters, the decay components of **Ia** monitored at short wavelength regions are always faster than those measured in **Ib** (see Figures 6, 7, and 9 for comparison). For example, the fast decay component at 500 nm was fitted to be 410 fs for **Ia** in CH_2Cl_2, which is nearly twice as fast as that of 760 fs measured in **Ib** (see Table 1). Second, when monitoring at longer wavelengths of >550 nm in, e.g., CH_2Cl_2, the rise dynamics in **Ib**, found to be resolvable and correlated with the solvent relaxation time, could no longer be resolved (i.e., <150 fs) in the case of **Ia**. The results cannot be rationalized by a model simply incorporating only solvent relaxation dynamics. Instead, an additional deactivation pathway incorporating ESIPT in **Ia**

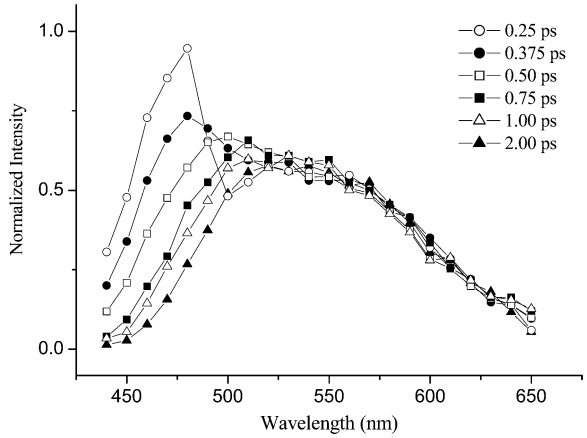

Figure 14. The temporal spectral evolution of **Ia** in dichloromathane. The solid lines express the corresponding fitted curves.

must play a key role for the observed dynamics in these solvents. Support of this viewpoint is rendered by extracting the spectral temporal evolution for **Ia**. As shown in Figure 14, the time-dependent spectral evolution acquired at an earlier time domain of <1.0 ps revealed two distinct bands maximized at 500 and ~530 nm in benzene, followed by a continuously time-dependent spectral red-shift toward a steady-state peak wavelength of ~560 nm in a period of ~1 ps. The result is in sharp contrast to the continuous, time-dependent spectral evolution solely due to the solvent relaxation in **Ib** (see Figure 9 for comparison), supporting the viewpoint in that a precursor−successor ESIPT must be involved in the deactivation processes for **Ia**.

4. Discussion

To view the above results on a fundamental basis, we have performed theoretical approaches based on the 6-31G(d′,p′) basis sets at a Hartree−Fock level. As a result, dipole moments for the geometry optimized **Ia** normal and tautomer species in the ground state were calculated to be 3.2 and 4.2 D, respectively, and the angle between these two dipole vectors was less than 15°. Conversely, as supported by the nearly solvent-polarity independent tautomer emission in **Ic** (see Figure 3), it is also reasonable to assume a similar dipole moment in terms of both magnitude and orientation between ground and excited states of the tautomer species. Accordingly, we can securely conclude that the excited proton-transfer tautomer possesses a similar dipolar character with respect to that of the normal ground state. The results, in combination with experimental data, lead us to propose a mechanism incorporating competitive proton-transfer versus solvent relaxation for **Ia**, depicted in Scheme 4.

Upon Franck−Condon excitation, **Ia** undergoes an instant, gigantic dipolar change due to the charge redistribution. Subsequently, the unfavorable polarization configuration is subject to a rapid solvent relaxation/reorientation to reach an energetically more favorable configuration. However, due to the identical polarization environments in the normal ground state and excited proton-transfer tautomer state, the solvent polarization effect should be decoupled from the ESIPT pathway at early times after the Franck−Condon excitation. If ESIPT is energetically allowed, proton transfer free of the solvent-polarity perturbation is expected. The rate of intrinsic ESIPT, which is normally dominated by the proton tunneling process, may be on the same magnitude as the rate of solvent relaxation, resulting in a competitive deactivation pathway. Because the fast decay

SCHEME 4: The Proposed Relaxation Dynamics of Ia as a Function of Solvent Polarities[a]

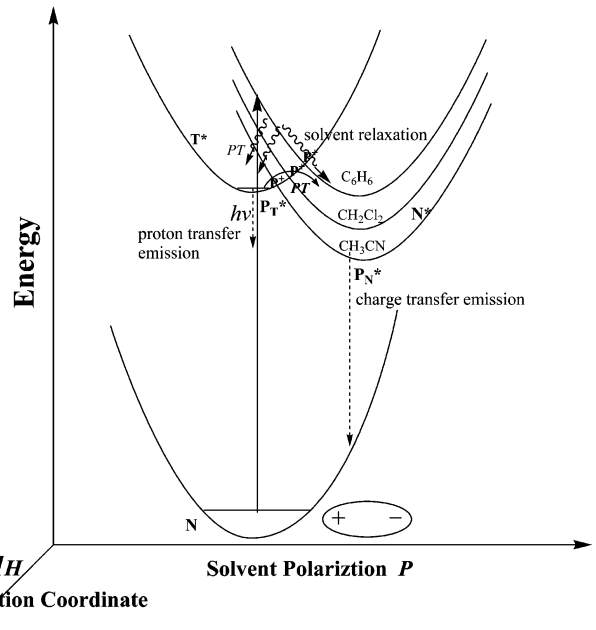

[a] *PT* denotes the solvent polarity perturbed proton-transfer process. P^*_N and P^*_T are the equilibrium polarization for N* and T*, respectively. P^+ represents the critical solvation configuration, in which the N* and P* are in the same energy. Note that the ground-state tautomer (T) is not shown in this scheme.

component of **Ia**, which is dominated by rates of ESIPT and solvation process, is on the order of a few hundred femtoseconds, the rate of ESIPT must be resolvable. For a simplified approach, the decay at a blue region of ~480 nm was fitted to be 780 and 410 fs for **Ib** and **Ia**, respectively, in CH_2Cl_2. Taking the solvent relaxation rate for both **Ia** and **Ib** to be the same, the rate of ESIPT is thus estimated to be ~860 fs^{-1}. The results are in contrast to the system response limited rate of ESIPT in the case of 2-hydroxylbenzaldehyde (**2HBA**),[25] indicating that the charge-transfer property in **Ia** leads to different distribution of the charge density from that of **2HBA**, so that the driving force (i.e. photoacidity and basicity, etc.) for ESIPT is appreciably reduced in **Ia**.

After reaching a critical solvation configuration, such as point P^+ depicted in Scheme 4, ESIPT becomes energetically uphill due to the unfavorable solvent polarization, so the deactivation subsequently should be dominated by the solvent relaxation, finally achieving a solvent-stabilized, equilibrated charge transfer state. As supported by the steady-state approach, in that the charge-transfer emission is predominant in benzene and dipolar solvents, the more stable one in the equilibrated excited state should be ascribed to the charge-transfer manifold. Thus, ESIPT from N* → T* after equilibrium population is energetically prohibited. Conversely, T* → N* reverse proton transfer, in which T* is populated originally from the early time domain, is expected to be thermodynamically allowed. Because of the different equilibrium polarization configuration between N* and T*, the solvent polarity effect is expected to incorporate into the ESIPT reaction pathway, resulting in a nonnegligible barrier.

If the coupling is small, the solvent-induced barrier in ESIPT may be described semiquantitatively by the Marcus theory,[26−29] commonly applied in the photoinduced electron transfer reaction, which simply predicts that the solvent-induced barrier ΔG^+ for the T* → N* proton-transfer reaction is related to the reaction exothermicity ΔG (see Scheme 1) and the solvent reorganization

energy λ, expressed as $\Delta G^+ = (\lambda/4)(1 + \Delta G/\lambda)^2$. λ may be obtained from an Onsager cavity model described as

$$\lambda = \frac{(\mu_N - \mu_T)^2}{a_0^3}\left(\frac{\epsilon_0 - 1}{2\epsilon_0 + 1} - \frac{\epsilon_\infty - 1}{2\epsilon_\infty + 1}\right)$$

where ϵ_∞ is the high-frequency dielectric constant, which is equivalent to the square of the refraction index n. ϵ_0 is the static dielectric constant and can be experimentally calculated from the Classius−Mossotti equation.[30] Consequently, a three-dimensional plot of free energy for ESIPT as a function of the solvent polarization coordinate P and the proton-transfer reaction coordinate q_H at solvation coordinates of excited tautomer (P^*_T), intermediate (P^+), and normal (P^*_N) is depicted in Scheme 4. The reaction coordinate q_H may turn out to be complicated due to numerous internal motions that may modulate the height and width of the proton-transfer barrier. The population with energy being equal to the solvent-induced barrier ΔG^+ is given by the Boltzman factor under the assumption that solvent relaxation in the reactant well is quite fast. For proton transfer to occur, this population must advance along the solvent coordinate P and hop from the reactant to the product surface. The latter process normally corresponds to tunneling through a barrier along the proton motion coordinate q_H. Two extreme limits can be considered to treat the overall reaction dynamics. Consider the first case, where tunneling through the q_H coordinate at $P = P^+$ is assumed to be relatively slow. In this case, crossing from the normal to the proton-transfer tautomer surface is quite unlikely. Since the coupling between the reactant and product coupling enters directly into the kinetic model, this expression is essentially analogous to the nonadiabatic electron transfer.[31] On the other hand, in the case where tunneling along the q_H coordinate is very fast, proton transfer from the normal to the tautomer species along the excited-state potential hypersurface occurs essentially every time the P^+ solvent configuration is achieved. In this case, the preexponential A factor is approximately equal to the inverse of the solvent longitudinal relaxation time (τ_L^{-1}) and is independent of the reactant/product coupling. This expression is analogous to adiabatic electron transfer, and the rate of ESIPT must be fast.

Because no slow rise (or decay) dynamics of $<10^{12}$ s^{-1} could be resolved, it is more likely that the ESIPT dynamics for **Ia** can be attributed to an adiabatic type of proton transfer, in which the solvent-induced barrier must be negligibly small. However, as indicated by Figures 11−13, because no rise dynamics attributed to the solvent relaxation can be resolved, we cannot rule out another possibility, that the lack of solvent-induced dynamics is due to the strong overlap between charge-transfer and proton-transfer emission. Furthermore, one has to be wary of applying the Marcus model in interpreting the proton-transfer reaction. The Marcus theory was originally derived for outer-sphere electron-transfer reactions in solution, which might not be a suitable model for dealing with the proton-transfer reaction. Particularly, proton transfer simultaneously involves bond breaking and making as well as strong electrostatic solute-surrounding solvent interaction. Nevertheless, several researchers[17,18] have stressed the importance of understanding how an equation whose structure is based on electron-transfer theory could be successful in the proton-transfer context, where the assumptions of electron-transfer theory do not apply. For example, electron-transfer theory generally assumes that the electronic coupling between reactant and product states is small (e.g., 1 kcal/mol or even less),[19] whereas for the proton transfer, a typical electronic coupling value might be on the order of an electronvolt.[20,21] In addition, a feature reflecting the absence of bond breaking/making in outer-sphere electron transfer is essentially present in the proton-transfer reaction. Recently, detailed discussion of the modified theory suited to acid−base ionization proton-transfer reaction in polar media has been reported by Kiefer and Hynes.[32,33] Since a proton-transfer hypersurface is much more complicated in the excited state, further details are not discussed in this study.

Finally, a large number of different mechanisms have been proposed to account for the *p*-*N*,*N*-dialkylaminobenzaldehyde types of molecules exhibiting anomalous charge-transfer emission.[34] Among these models, the most widely accepted one is based on the mechanism incorporating twisted intramolecular charge transfer (TICT). One main debatable controversy for TICT lies in whether these molecules twist or not during the charge-transfer process.[35,36] Unfortunately, the femtosecond relaxation dynamics presented here could not resolve any dynamics associated with the rotational motion of **Ia**. On one hand, the electronic coupling between ditolyl amino (donor) and formaldehyde (acceptor) through the π conjugation might be very strong, such that the instant electron rearrangement, i.e., optical transfer, takes place. On the other hand, it is notable that the TICT model incorporating a rigid and perpendicular geometry is only an idealized limiting case, and the reality involves broad angular distributions centered around perpendicular twist angles.[35] In addition, there is a reservation if the electron donor subgroup is completely decoupled from the acceptor subgroup in the ICT state. According to an ab initio approach (6-31G(d′,p′) basis sets at a Hartree−Fock level), the geometrically optimized structures for both **Ia** and **Ib** possess a large twist angle of ∼40° in the ground state. Due to the pretwisted angle in the ground state, **Ia** and **Ib** may undergo ultrafast charge transfer, i.e., charge redistribution, in the excited sate, of which the dynamics of the partially decoupled species are not resolvable in this work due to the system response of 150 fs. Focus on determining the possible twist motion coupled charge-transfer process is currently in progress.

5. Conclusion

In conclusion, we report on the excitation behaviors for charge versus proton transfer for **Ia** and its related derivatives (**Ib**−**c**). In cyclohexane, near isoenergetics are established between charge-transfer (normal) and proton-transfer states for **Ia**. The excited charge-transfer state, possessing gigantic dipole moment change with respect to the ground state, is further stabilized via a solvent relaxation process. In benzene and dipolar solvents, the rates of ESIPT and solvent relaxation are competitive, and the populated charge-transfer state is thermodynamically favorable. Once the proton-transfer tautomer is populated, an adiabatic, fast excited-state reverse proton transfer takes place. The solvent polarity induced barrier is concluded to be small, such that the reaction rate is approximately equal to the inverse of the solvent longitudinal relaxation time and is independent of the reactant/product coupling. The results are in sharp contrast to system **II**, based on 3-hydroxyflavone derivatives, in which the intrinsic proton-tunneling rate has been proposed to be relatively much slower than the solvent relaxation dynamics and in which the solvent coupling effect strongly affects the ESIPT dynamics.[10] It is thus also intriguing to examine the associated solvent polarity coupled ESIPT dynamics for 3-hydroxyflavone based system **II** analogues in the early time domain. Focus on this issue is currently in progress.

References and Notes

(1) In general, it is difficult to distinguish the mechanism between proton transfer and hydrogen atom transfer reactions. In this review article we simply adopted the conventional term namely "proton transfer" throughout the text, which is particularly more suitable in describing the solvent polarity coupled proton-transfer tautomerism.

(2) For example, see: *Studies in Physical and Theoretical Chemistry*; Müller, A., Ratajack, H., Junge, W., Diemann, E., Eds.; Electron and Proton Transfer in Chemistry and Biology, Vol. 78; Elsevier: Amsterdam, The Netherlands, 1992.

(3) (a) Scheiner, S. *J. Phys. Chem. A* **2000**, *104*, 5898. (b) Waluk, J. Conformational Aspects of Intra- and Intermolecular Excited-State Proton Transfer. In *Conformational Analysis of Molecules in Excited States*; Waluk, J., Ed.; Wiley-VCH: New York, 2000. (c) Chou, P. T. *J. Chin. Chem. Soc.* **2001**, *48*, 651. (d) Wu, K.-C.; Cheng, Y.-M.; Lin, Y.-S.; Yeh, Y.-S.; Pu, S.-C.; Hu, Y.-H.; Yu, J.-K.; Chou, P.-T. *Chem. Phys. Lett.* **2004**, *382*, 203. (e) Paterson, M. J.; Robb, M. A.; Blancafort, L.; DeBellis, A. D. *J. Am. Chem. Soc.* **2004**, *126*, 2912. (f) Lochbrunner, S.; Wurzer, A. J.; Riedle, E. *J. Phys. Chem. A* **2003**, *107*, 10580. (g) de Vivie-Riedle, R.; De Waele, V.; Kurtz, L.; Riedle, E. *J. Phys. Chem. A* **2003**, *107*, 10591. (h) Shynkar, V. V.; Mely, Y.; Duportail, G.; Piemont, E.; Klymchenko, A. S.; Demchenko, A. P. *J. Phys. Chem. A* **2003**, *107*, 9522. (i) Cheng, C.-C.; Chang, C.-P.; Yu, W.-S.; Hung, F.-T.; Liu, Y.-I.; Wu, G.-R.; Chou, P.-T. *J. Phys. Chem. A* **2003**, *107*, 1459. (j) Lukeman, M.; Wan, P. *J. Am. Chem. Soc.* **2003**, *125*, 1164.

(4) In some ESIPT molecules, the lowest excited singlet state is in an $n\pi^*$ configuration, in which ESIPT is prohibited. For a recent review, see ref 3a.

(5) ESIPT incorporating phenol O−H to a β-carbon atom is not included in this category, see: Lukeman, M.; Wan, P. *J. Am. Chem. Soc.* **2002**, *124*, 9458.

(6) For recent examples, see: (a) Chudoba, C.; Riedle, E.; Pfeiffer, M.; Elsaesser, T. *Chem. Phys. Lett.* **1996**, *263*, 622. (b) Lochbrunner, S.; Wurzer, A. J.; Riedle, E. *J. Chem. Phys.* **2000**, *112*, 10699. (c) Chou, P.-T.; Chen, Y.-C.; Yu, W.-S.; Chou, Y.-H.; Wei, C.-Y.; Cheng, Y.-M. *J. Phys. Chem. A* **2001**, *105*, 1731. (d) Ameer-Beg S.; Ormson, S. M.; Brown, R. G.; Matousek, P.; Towrie, M.; Nibbering, E. T. J.; Foggi, P.; Neuwahl, F. V. R. *J. Phys. Chem. A* **2001**, *105*, 3709. (e) Chou, P.-T.; Chen, Y.-C.; Yu, W.-S.; Cheng, Y.-M. *Chem. Phys. Lett.* **2001**, *340*, 89.

(7) For examples, see: (a) McMorrow, D.; Kasha, M. *J. Phys. Chem.* **1984**, *88*, 2235. (b) Brucker, G. A.; Kelley, D. F. *J. Phys. Chem.* **1987**, *91*, 2856. (c) Brucker, G. A.; Kelley, D. F. *J. Phys. Chem.* **1987**, *91*, 2862. (d) Strandjord, A. J. G.; Barbara, P. F. *J. Phys. Chem.* **1985**, *89*, 2355. (e) Brucker, G. A.; Kelley, D. F.; Swinney, T. C. *J. Phys. Chem.* **1991**, *95*, 3190.

(8) (a) Gormin, D.; Kasha, M. *Chem. Phys. Lett.* **1988**, *153*, 574. (b) Heldt, J.; Gormin, D.; Kasha, M. *Chem. Phys.* **1989**, *136*, 321.

(9) (a) Chou, P.-T.; Martinez, M. L.; Clements, J. H. *J. Phys. Chem.* **1993**, *97*, 2618. (b) Chou, P.-T.; Martinez, M. L.; Clements, J. H. *Chem. Phys. Lett.* **1993**, *204*, 395.

(10) (a) Swinney, T. C.; Kelley, D. F. *J. Chem. Phys.* **1993**, *99*, 211. (b) Parsapour, F.; Kelley, D. F. *J. Phys. Chem.* **1996**, *100*, 2791.

(11) Ormson, S. M.; Brown, R. G.; Vollmer, F.; Rettig, W. *J. Photochem. Photobiol. A* **1994**, *81*, 65.

(12) For examples, see: (a) Studer, S. L.; Brewer, W. E.; Martinez, M. L.; Chou, P.-T. *J. Am. Chem. Soc.* **1989**, *111*, 7643. (b) Chou, P.-T.; Studer, S. L.; Martinez, M. L.; Orton, E.; Young, M. *Photochem. Photobiol.* **1991**, *53*, 587.

(13) Chou, P.-T.; Chen, Y.-C.; Yu, W.-S.; Chou, Y.-H.; Wei, C.-Y.; Cheng, Y.-M. *J. Phys. Chem. A* **2001**, *105*, 1731.

(14) Frisch, M. J.; Trucks, G. W.; Schlegel, H. B.; Scuseria, G. E.; Robb, M. A.; Cheeseman, J. R.; Zakrzewski, V. G.; Montgomery, J. A., Jr.; Stratmann, R. E.; Burant, J. C.; Dapprich, S.; Millam, J. M.; Daniels, A. D.; Kudin, K. N.; Strain, M. C.; Farkas, O.; Tomasi, J.; Barone, V.; Cossi, M.; Cammi, R.; Mennucci, B.; Pomelli, C.; Adamo, C.; Clifford, S.; Ochterski, J.; Petersson, G. A.; Ayala, P. Y.; Cui, Q.; Morokuma, K.; Malick, D. K.; Rabuck, A. D.; Raghavachari, K.; Foresman, J. B.; Cioslowski, J.; Ortiz, J. V.; Stefanov, B. B.; Liu, G.; Liashenko, A.; Piskorz, P.; Komaromi, I.; Gomperts, R.; Martin, R. L.; Fox, D. J.; Keith, T.; Al-Laham, M. A.; Peng, C. Y.; Nanayakkara, A.; Gonzalez, C.; Challacombe, M.; Gill, P. M. W.; Johnson, B.; Chen, W.; Wong, M. W.; Andres, J. L.; Gonzalez, C.; Head-Gordon, M.; Replogle, E. S.; Pople, J. A. *GAUSSIAN* 98, Revision A.7; Gaussian, Inc.: Pittsburgh, PA, 1998.

(15) (a) Nagaoka, S. I.; Hirota, N.; Sumitani, M.; Yoshihara, K. *J. Am. Chem. Soc.* **1983**, *105*, 4220. (b) Toribio, F.; Catalán, J.; Amat, F.; Acuña, A. U. *J. Phys. Chem.* **1983**, *87*, 817.

(16) Stock, K.; Bizjak, T.; Lochbrunner, S. *Chem. Phys. Lett.* **2002**, *354*, 409.

(17) Lippert, E. *Z. Naturforsch.* **1955**, *10a*, 541.

(18) Mataga, N.; Kubota, T. *Molecular Interactions and Electronic Spectra*; Marcel Dekker: New York, 1970; p *385*.

(19) Bilot, L.; Kawski, A. *Z. Naturforsch.* **1962**, *17a*, 621.

(20) Liptay, W. *Z. Naturforsch.* **1965**, *20a*, 1441.

(21) Lakowicz, J. R. *Principles of Fluorescence Spectroscopy*; Plenum Press: New York, 1983.

(22) (a) Nagarajan, V.; Brearley, A. M.; Kang, T. J.; Barbara, P. F. *J. Chem. Phys.* **1987**, *86*, 3183. (b) Barbara, P. F.; Jarzeba, W. *Adv. Photochem.* **1990**, *15*, 1.

(23) Horng, M. L.; Gardecki, J. A.; Papazyan, A.; Maroncelli, M. *J. Phys. Chem.* **1995**, *99*, 17311.

(24) Reynolds, L.; Gardecki, J. A.; Frankland, S. J. V.; Horng, M. L.; Maroncelli, M. *J. Phys. Chem.* **1996**, *100*, 10337.

(25) Stock, K.; Bizjak, T.; Lochbrunner, S. *Chem. Phys. Lett.* **2002**, *354*, 409.

(26) Marcus, R. A. *J. Chem. Phys.* **1965**, *43*, 379.

(27) Marcus, R. A. *Annu. Rev. Phys. Chem.* **1964**, *15*, 155.

(28) Marcus, R. A. *J. Chem. Phys.* **1965**, *43*, 679.

(29) Marcus, R. A. *Rev. Mod. Phys.* **1993**, *65*, 599.

(30) Bordewijk, O. *Theory of Electric Polarization*; Elsevier: Amsterdam, The Netherlands, 1978; Vol. 2.

(31) Calef, D. F.; Wolynes, P. G. *J. Phys. Chem.* **1983**, *87*, 3387.

(32) Kiefer, P. M.; Hynes, J. T. *J. Phys. Chem. A* **2002**, *106*, 1834.

(33) Kiefer, P. M.; Hynes, J. T. *J. Phys. Chem. A* **2002**, *106*, 1850.

(34) (a) Weisenborn, P. C. M.; Huizer, A. H.; Varma, C. A. G. O. *J. Chem. Soc., Faraday Trans.* **1989**, *85*, 1895. (b) Blib, B.; Lommatzsch, U.; Monte, C.; Rettig, W.; Brutschy, B. *Chem. Phys.* **2000**, *254*, 407.

(35) Rettig, W.; Zietz, B. *Chem. Phys. Lett.* **2000**, *317*, 187.

(36) Rappoport, D.; Furche, F. *J. Am. Chem. Soc.* **2004**, *126*, 1279.